Soft Matter

ARTICLE TYPE

Cite this: DOI: 10.1039/xxxxxxxxxx

SI:Experimental Observation of Near-Wall Effects During the Puncture of Soft Solids

Christopher W. Barney,[a,b,c] Szabolcs Berezvai,[d] Allison L. Chau,[e] Younghoon Kwon,[b] Angela A. Pitenis,[e] Robert M. McMeeking,[b,e] Megan T. Valentine,[b*] and Matthew E. Helgeson[a*]

Received Date
Accepted Date

DOI: 10.1039/xxxxxxxxxx

www.rsc.org/journalname

1 Deep Indentation and Puncture

Summary data for the trials with variable sample height are contained in Table S1. Summary data for the variable velocity trials are contained in Table S2. An enlarged version of Figure 1 from the main text is shown in Figure S1. Expanded versions of the plots of force vs Ed^2 from Figure 2 in the main text are contained in Figure S2, Figure S3, and Figure S4. Similarly, the force displacement plots from Figure 4a are shown in Figure S5.

[a] *Department of Chemical Engineering, University of California Santa Barbara, Santa Barbara, CA 93106, USA.*
[b] *Department of Mechanical Engineering, University of California Santa Barbara, Santa Barbara, CA 93106, USA.*
[c] *Current Address: School of Polymer Science and Polymer Engineering, University of Akron, Akron OH, 44325, USA.*
[d] *Department of Applied Mechanics, Faculty of Mechanical Engineering, Budapest University of Technology and Economics, Műegyetem rkp. 3., H-1111 Budapest, Hungary*
[e] *Materials Department, University of California Santa Barbara, Santa Barbara, CA 93106, USA.*
[*] *Corresponding Authors Email: helgeson@ucsb.edu, valentine@engineering.ucsb.edu*
‡ Additional footnotes to the title and authors can be included *e.g.* 'Present address:' or 'These authors contributed equally to this work' as above using the symbols: ‡, §, and ¶. Please place the appropriate symbol next to the author's name and include a `\footnotetext` entry in the the correct place in the list.

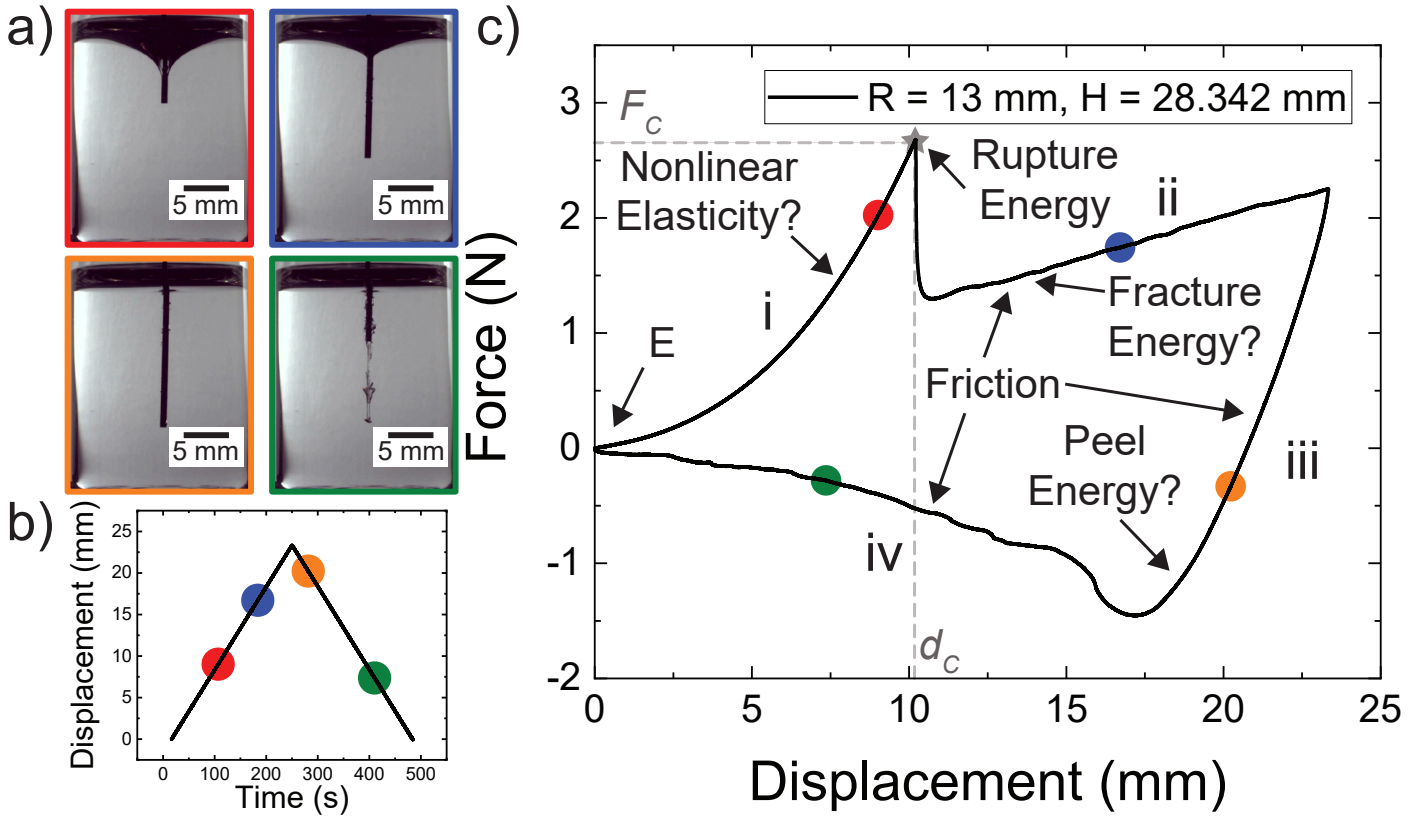

Fig. S1 An enlarged version of Figure 1 from the main text. a) Images during the four stages of deep indentation and puncture from a representative run in a vial performed with a sample radius of 13 mm and height of 28.342 mm at a displacement rate of 0.1 mm/s. b) Plot of the imposed displacement against time with the image locations marked via colored circles. c) Plot of the measured force against displacement during deep indentation and puncture with the four stages of this test marked (i-iv). The critical puncture force F_c and displacement d_c are marked by the grey star and dashed lines. Additionally, the mechanical behavior that can be characterized during each stage has been labeled with underexplored areas denoted by question marks.

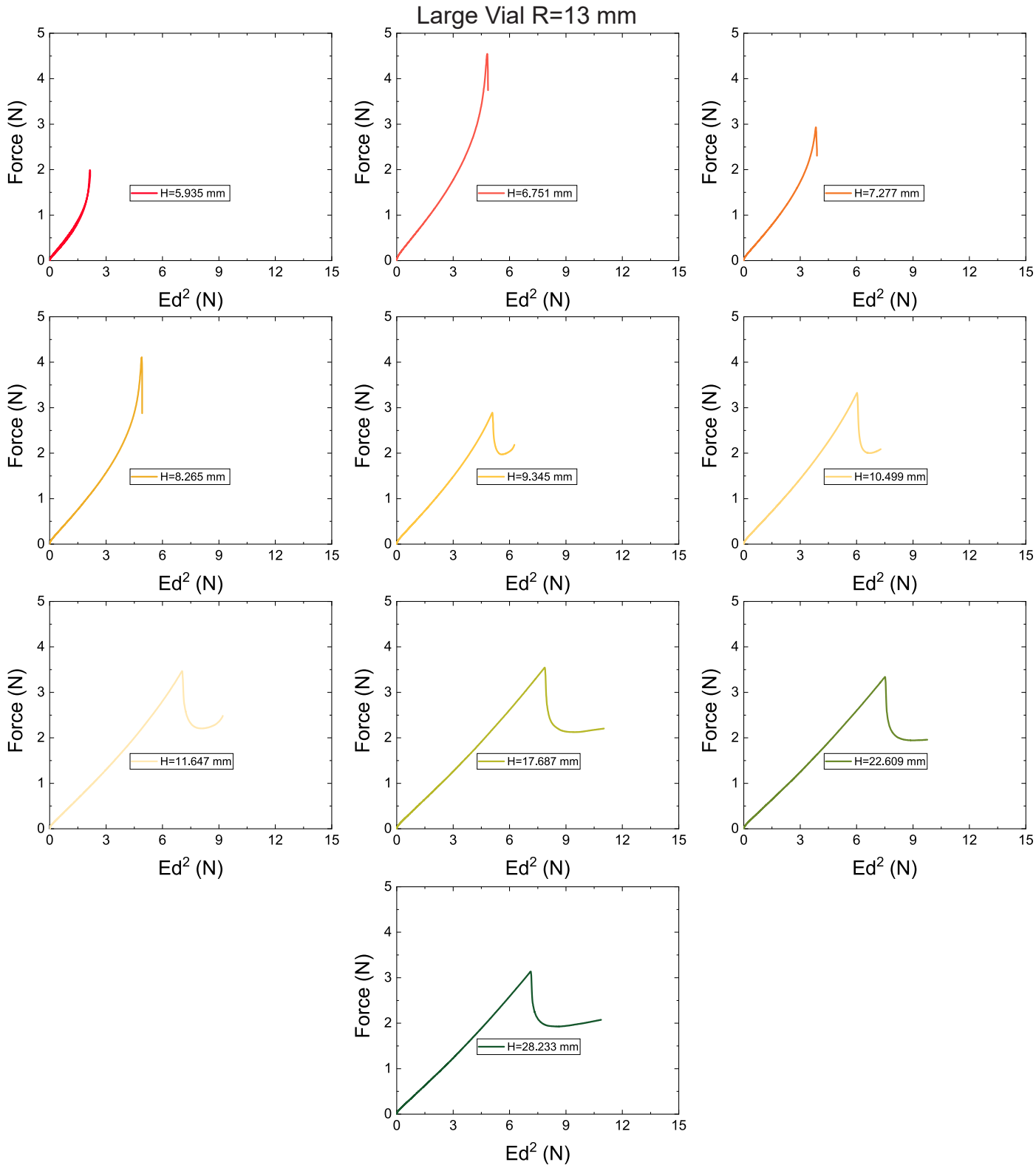

Fig. S2 Expanded plots from Figure 2a in the main text.

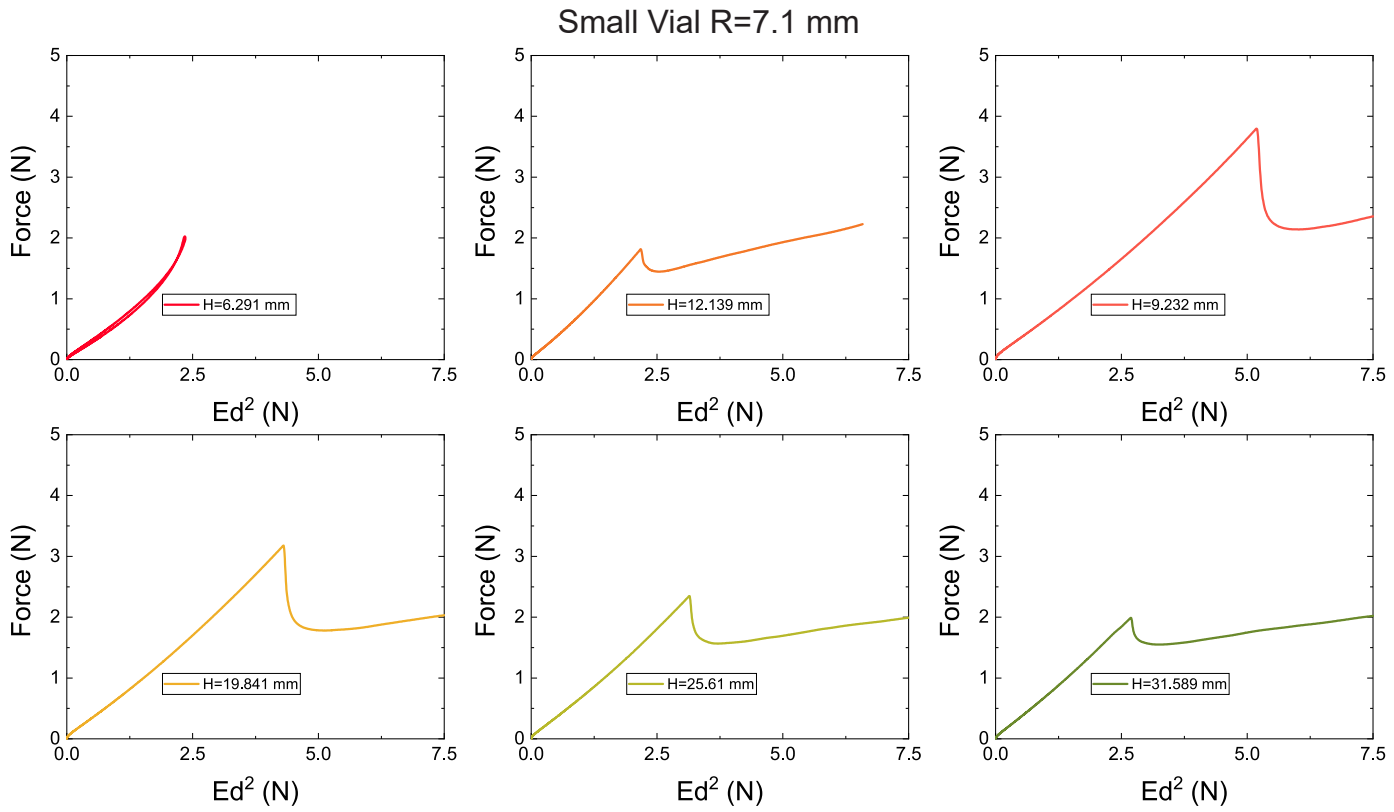

Fig. S3 Expanded plots from Figure 2b in the main text.

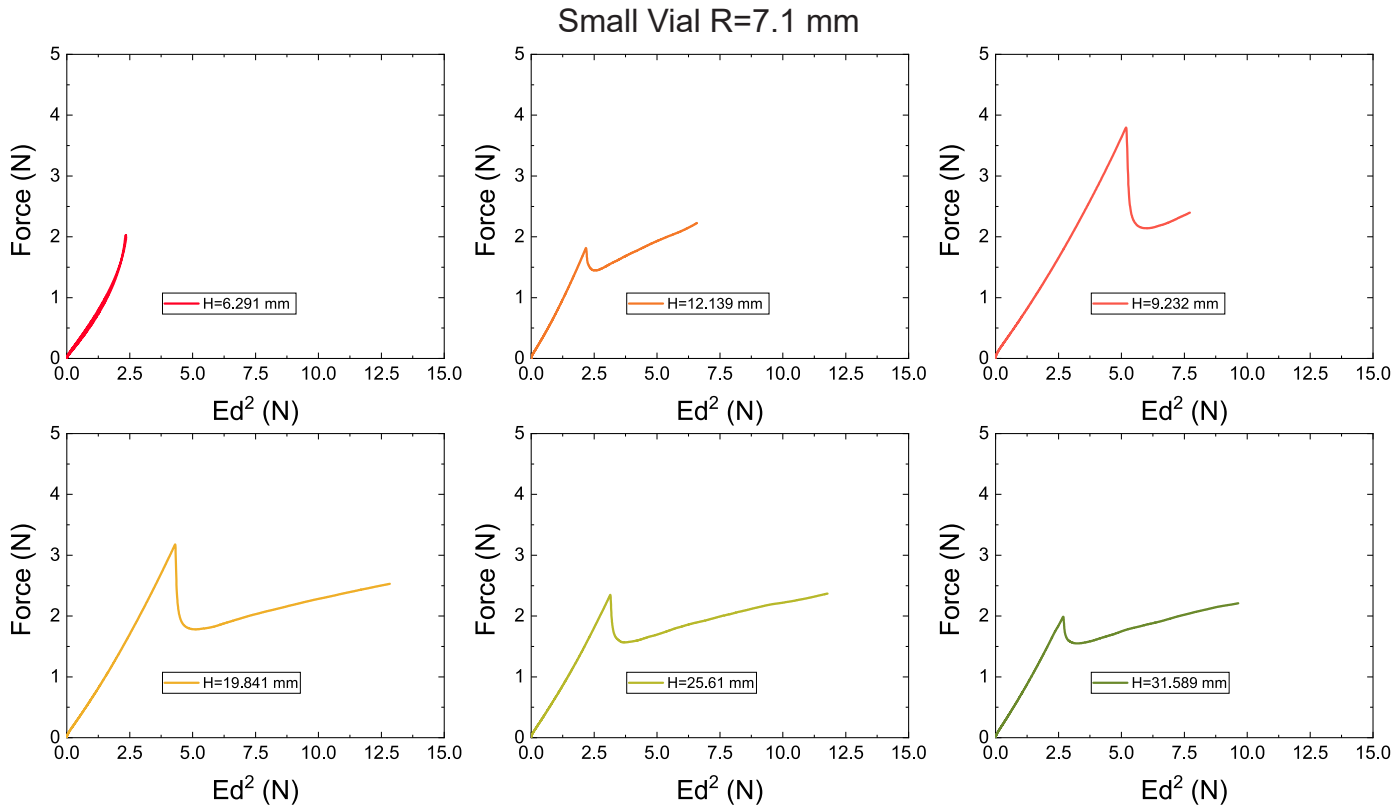

Fig. S4 Expanded plots from Figure 2b in the main text with the same x axis as Figure 2a.

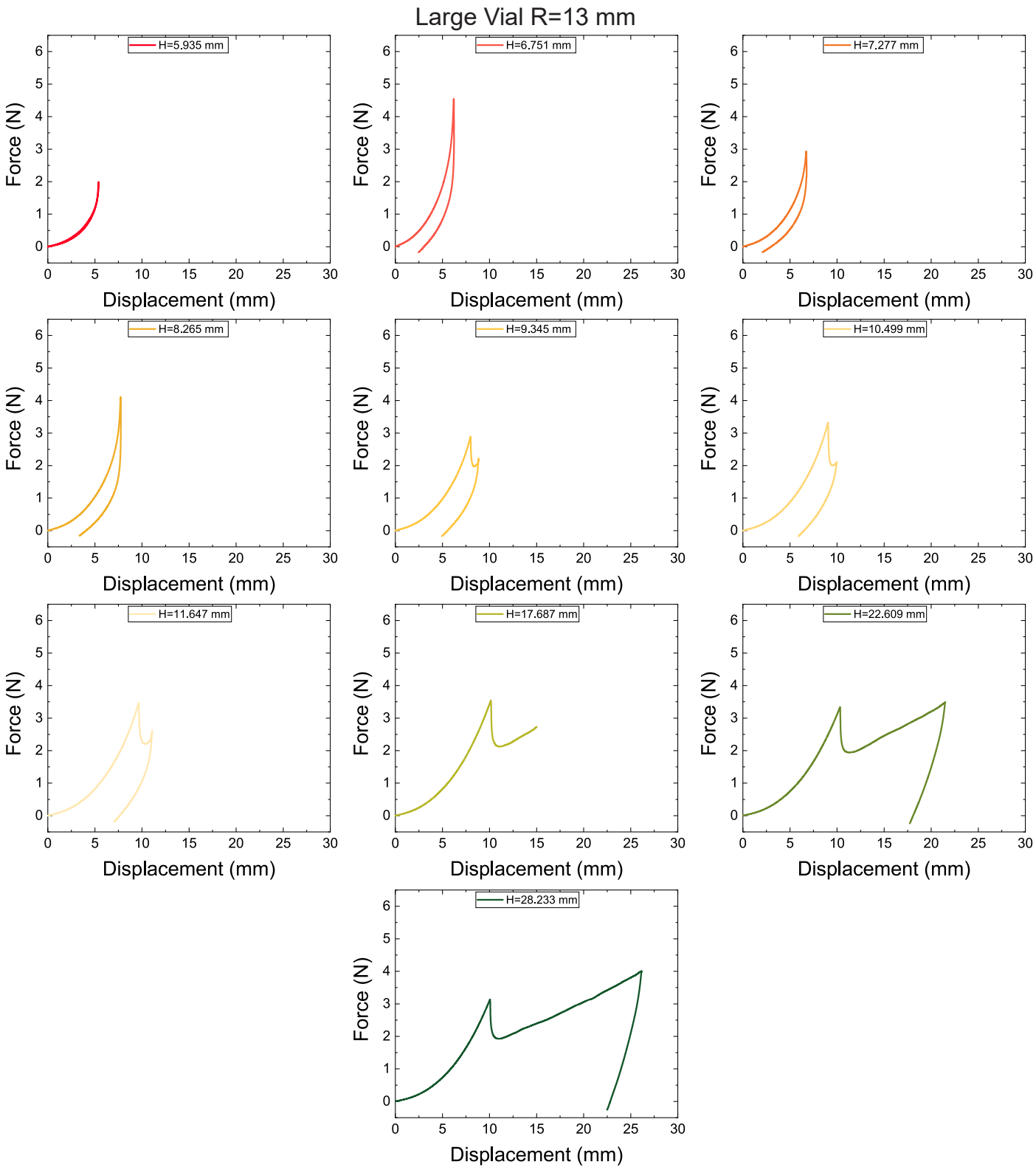

Fig. S5 Expanded plots from Figure 4a in the main text.

Table S1 Summary of the variable height deep indentation and puncture data gathered in this work. R, H, and E were quantified by small strain indentation. NP stands for no puncture and T stands for tubular.

Sample	R (mm)	a (mm)	H (mm)	E (kPa)	d_c (mm)	F_c (N)	Crack Morphology
Big3-1	13	0.359	5.935	73.6	5.435	–	NP
Big3-2	13	0.359	5.723	65.1	5.224	–	NP
Big3-3	13	0.359	5.663	73.4	5.150	–	NP
Big3.5-1	13	0.359	6.751	125.9	6.224	4.5425	T
Big3.5-2	13	0.359	6.718	126.9	6.013	4.5505	T
Big3.5-3	13	0.359	6.604	116.1	5.564	2.2113	T
Big4-1	13	0.359	7.277	84.8	6.723	2.9328	T
Big4-2	13	0.359	7.365	82.3	6.863	3.4357	T
Big4-3	13	0.359	7.494	88.4	6.979	–	NP
Big4.5-1	13	0.359	8.265	81.8	7.751	4.1103	T
Big4.5-2	13	0.359	8.367	81.7	7.662	3.0451	T
Big4.5-3	13	0.359	8.309	80.2	7.773	3.7672	T
Big5-1	13	0.359	9.345	79.8	7.970	2.8921	T
Big5-2	13	0.359	9.492	80.6	7.854	2.6244	T
Big5-3	13	0.359	9.613	83.3	8.281	3.2131	T
Big5.5-1	13	0.359	10.499	73.6	9.051	3.3271	T
Big5.5-2	13	0.359	10.503	71.8	8.459	2.7294	T
Big5.5-3	13	0.359	10.658	75.8	8.321	2.5889	T
Big6-1	13	0.359	11.647	75.6	9.712	3.4684	T
Big6-2	13	0.359	11.058	73.0	8.744	2.7186	T
Big6-3	13	0.359	11.598	75.9	8.556	2.5402	T
Big9-1	13	0.359	17.687	76.4	10.194	3.5457	T
Big9-2	13	0.359	17.129	72.8	9.917	3.1367	T
Big9-3	13	0.359	16.838	68.5	9.645	2.7165	T
Big12-1	13	0.359	22.609	70.5	10.429	3.3383	T
Big12-2	13	0.359	22.996	67.1	8.298	1.9307	T
Big12-3	13	0.359	22.551	66.4	9.579	2.5394	T
Big15-1	13	0.359	28.233	70.5	10.143	3.1384	T
Big15-2	13	0.359	28.358	66.8	7.13	1.3813	T
Big15-3	13	0.359	28.069	67.7	10.878	3.5208	T
Small1-1	7.1	0.359	6.291	68.8	5.778	–	NP
Small1-2	7.1	0.359	6.180	65.6	5.673	–	NP
Small1-3	7.1	0.359	6.406	64.8	5.899	–	NP
Small1.5-1	7.1	0.359	9.232	102.0	7.162	3.7982	T
Small1.5-2	7.1	0.359	8.987	69.7	7.810	3.1123	T
Small1.5-3	7.1	0.359	10.080	58.1	8.126	2.8328	T
Small2-1	7.1	0.359	12.139	49.0	6.708	1.8158	T
Small2-2	7.1	0.359	12.105	66.7	7.119	2.3718	T
Small2-3	7.1	0.359	13.222	65.9	8.003	3.1207	T
Small3-1	7.1	0.359	19.841	67.9	8.007	3.1767	T
Small3-2	7.1	0.359	18.749	66.6	7.935	2.9940	T
Small3-3	7.1	0.359	18.629	59.4	7.830	2.8569	T
Small4-1	7.1	0.359	25.610	64.6	7.035	2.3476	T
Small4-2	7.1	0.359	25.618	63.4	7.181	2.5027	T
Small4-3	7.1	0.359	25.661	65.4	7.099	2.3942	T
Small5-1	7.1	0.359	31.589	61.4	6.626	1.9887	T
Small5-2	7.1	0.359	31.662	58.0	7.668	2.8192	T
Small5-3	7.1	0.359	30.830	61.9	7.613	2.8224	T
EXT	23.5	0.359	30	33.053	12.4	1.69118	T
EXT	23.5	0.359	30	32.46	14.2	2.24488	T
EXT	23.5	0.359	30	32.15	13.2	1.8895	T

Table S2 Summary of the variable velocity deep indentation and puncture data gathered in this work.

Sample	R (mm)	a (mm)	Velocity (mm/s)	d_c (mm)	F_c (N)	$\frac{\partial F}{\partial d}$ (N/m)	F_{prop} (mN)
Big15-1	13	0.359	0.1	10.370	2.7164	61.08	542.1
Big15-2	13	0.359	0.1	10.192	2.6818	78.48	439.5
Big15-3	13	0.359	0.1	10.193	2.6892	71.43	620.6
Big15-4	13	0.359	0.1	10.263	2.7757	90.18	388.1
Big15-5	13	0.359	1	9.081	2.0110	119.07	353.3
Big15-6	13	0.359	1	8.953	1.9078	130.20	218.65
Big15-7	13	0.359	1	8.837	1.9389	135.84	190.67
Big15-8	13	0.359	1	9.150	2.1710	128.18	338.20
Big15-9	13	0.359	10	9.564	2.4996	221.88	-122.82
Big15-10	13	0.359	10	9.714	2.4217	226.43	-236.61
Big15-11	13	0.359	10	9.262	2.5171	242.14	-315.70
Big15-12	13	0.359	10	9.812	2.6215	224.97	-81.42
Small5-1	13	0.359	0.1	8.904	2.8749	20.00	988.00
Small5-2	13	0.359	0.1	8.752	2.7280	40.71	488.73
Small5-3	13	0.359	0.1	8.694	2.8867	10.73	1116.96
Small5-4	13	0.359	0.1	8.231	2.6306	55.87	464.21
Small5-5	13	0.359	1	7.595	2.3455	95.02	718.33
Small5-6	13	0.359	1	7.179	1.9256	121.76	471.58
Small5-7	13	0.359	1	7.283	1.8827	114.52	523.89
Small5-8	13	0.359	1	8.038	2.5896	95.08	836.18
Small5-9	13	0.359	10	7.015	2.0167	238.49	112.38
Small5-10	13	0.359	10	7.714	2.4634	242.46	-72.00
Small5-11	13	0.359	10	7.712	2.7328	216.61	218.87
Small5-12	13	0.359	10	7.065	2.1950	229.74	168.77

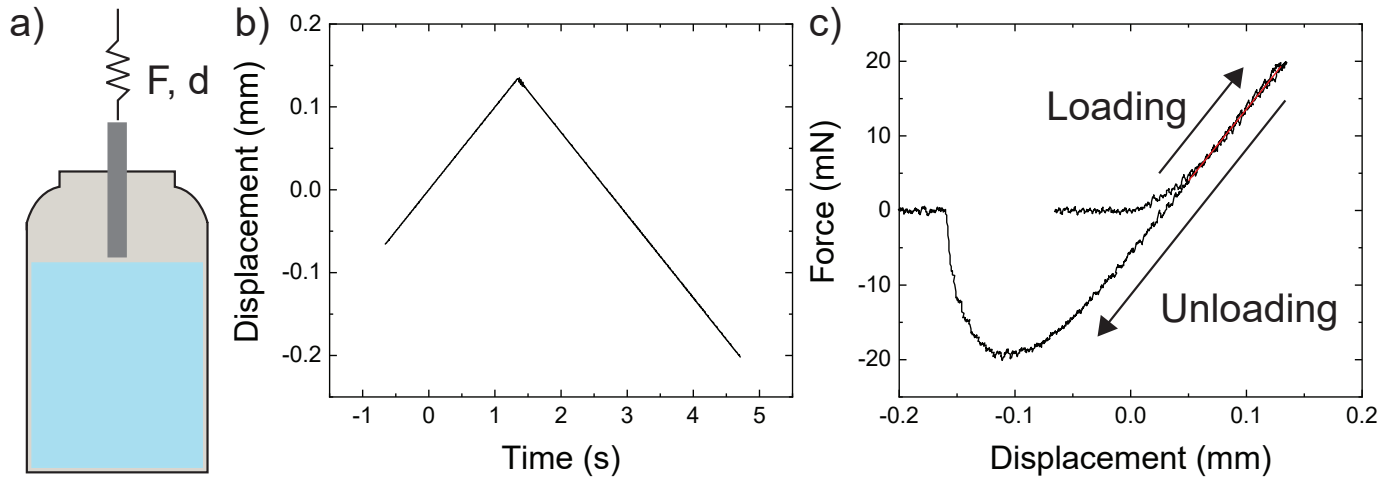

Fig. S6 a) A schematic of the setup used for performing small strain indentation. b) An example plot of the imposed displacement vs time curve for small strain indentation using a 2 mm diameter steel cylinder on a gel with $R = 13$ mm and $H = 28.233$ mm. c) A example plot of the force-displacement curve for the same sample showing how the stiffness ($S = 191.8 \pm 0.9$ N/m) is extracted from this curve.

2 Additional Characterization

2.1 Small Strain Indentation

Deep indentation and puncture were performed on a TA.XTPlus Connect Texture Analyzer with a 50 N load cell. Large vials were tested with a 2 mm diameter ($a = 1$ mm) flat cylindrical probe and small vials were tested with the 22 gauge (inner and outer radius of 0.207 mm and $a = 0.359$ mm, respectively) blunt-tipped steel needle used during puncture measurements. Measurements were performed at a displacement rate of 0.1 mm/s to a turnaround force of 20 mN. A schematic of the setup and plots of representative data are shown in Figure S6. The displacement shown in these plots has been shifted so that the zero point is defined by the initial point of contact between the probe and the material. The initial location of the probe was noted before running each test and was combined with the initial contact displacement to infer the sample height H values reported in Table S1.

Values of E were extracted from these measurements using the observed sample stiffness S, obtained from the slope of the red fit line Figure S6C. This stiffness can be used in combination with sample dimensions to calculate E using,[1]

$$E = \frac{3S}{8a}\left[1 + 1.33\frac{a}{H} + 1.33\left(\frac{a}{H}\right)^3\right]^{-1}, \tag{S1}$$

which combines classic Hertzian contact mechanics with a correction factor for the finite axial size of the sample (approximately 1 for all sample heights tested). E values calculated in this manner are reported in Table S1.

Plots of the sample volume V against the resulting sample height are contained in Figure S7. The slope on this plot is defined by the relationship,

$$\frac{V}{H} = \pi R^2, \tag{S2}$$

where R is the radius of the sample. These fits indicate that $R =$ 7.1 mm and $R = 13$ mm in the small and large vials, respectively.

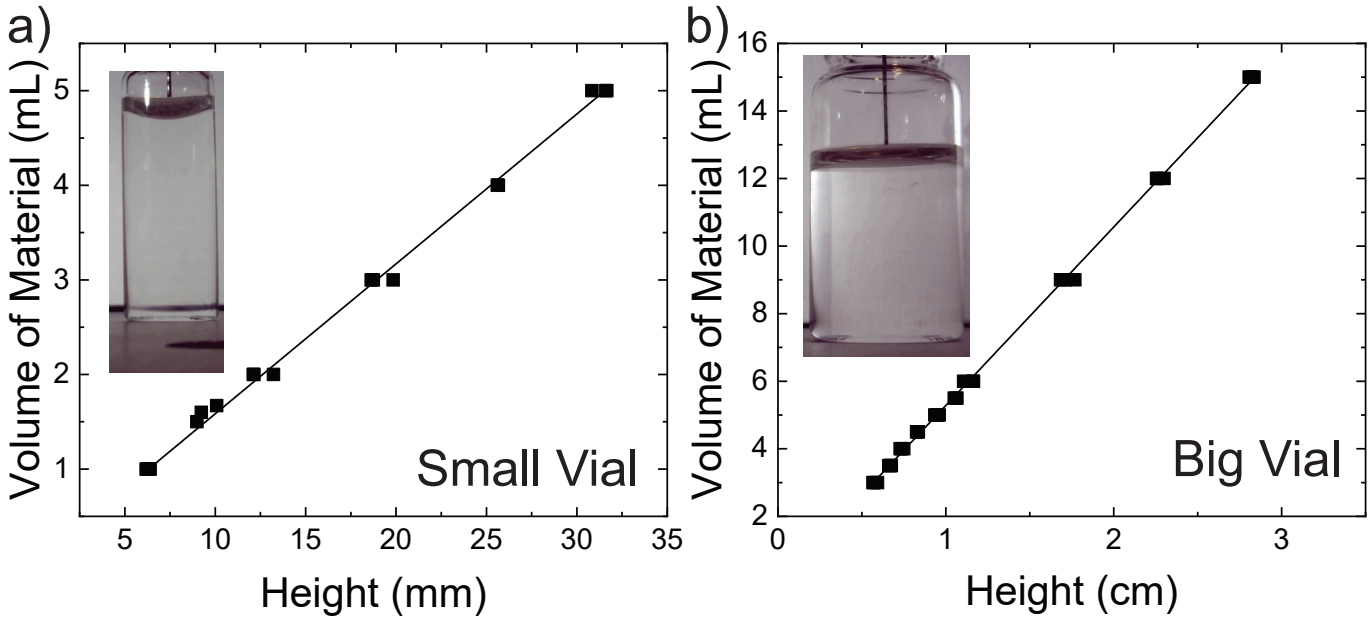

Fig. S7 Plots of the volume of material used to make samples against the measured sample height for the a) small and b) big vial. The fitted slope for the small (0.1585 ± 0.0009 mL/mm) and big (5.28 ± 0.02 mL/cm) were used to infer internal vial radius values of $R = 7.1$ mm and $R = 13$ mm using Equation (S2).

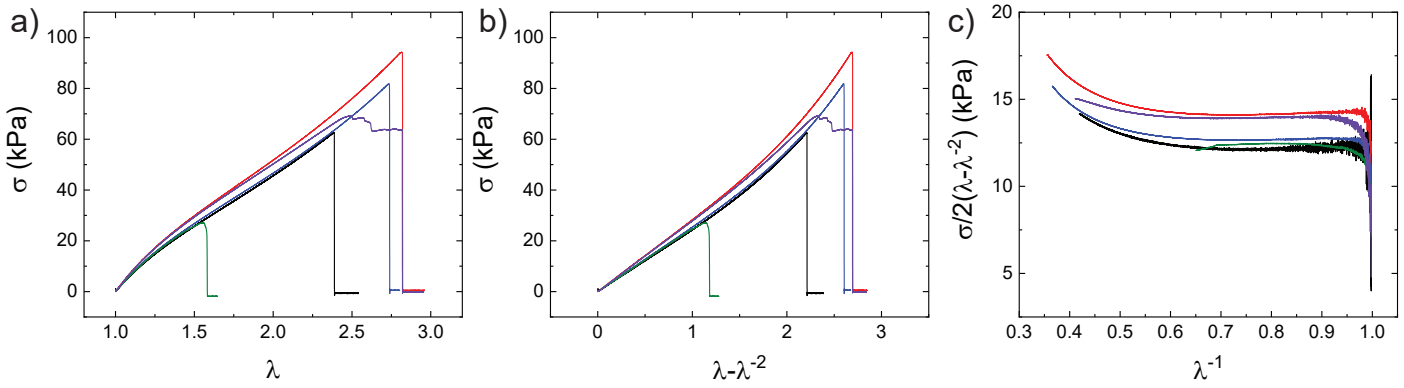

Fig. S8 Plots of the engineering stress σ against a) λ and b) $\lambda - \lambda^{-2}$ for uniaxial extension. Additionally a Mooney plot is contained in c). These tests suggest that this material displays some strain stiffening and little to no dependence on the $\frac{dW}{dI_2}$ term.

2.2 Constitutive Response

2.2.1 Uniaxial Extension

Uniaxial extension was performed on a TA.XTPlus Connect Texture Analyzer with a 50 N load cell and monitored with a Dino-Lite Edge Plus AM4117 series 1.3 MP camera. Measurements were performed on rectangular strips that maintained a length to width ratio of at least three for all samples. Samples were stretched at a velocity of 1 mm/s (approximate strain rate of 0.025 s^{-1}) until sample failure or slip at the clamp occurred.

Different representations of these measurements in the form of plots of a) the engineering stress σ vs stretch ratio λ, b) σ vs $\lambda - \lambda^{-2}$, and c) $\frac{\sigma}{2(\lambda - \lambda^{-2})}$ vs λ^{-1} are shown in Figure S8. The large spread observed in the ultimate failure strain is likely caused by the use of rectangular strips instead of dogbone shaped samples, which allows stress concentrations at the clamp to influence the failure point. E reported in the main text was extracted from the initial linear region of plot b) where the slope is $\frac{E}{3}$.[2] The plot in b) is used for this because the fit can be extracted from data up to $\sim 50\%$ strain instead of the $\sim 10\%$ strain (where the experimental errors can be large) that is usable from the plot in a). The Mooney plot representation[3,4] in c) highlights that significance of these errors in the first $5-10\%$. The horizontal plateau observed once these errors become negligible suggests that this material has little to no dependence on the $\frac{dW}{dI_2}$ in tension. Some strain stiffening of the samples is apparent in all three representations.

Data from cyclic extension measurements is shown in Figure S9. A sample was strained at a rate of 1 mm/s (0.03 s^{-1}) to a maximum turnaround strain for 5 cycles before the strain was increased for a further 5 cycles; this process was repeated with incremental increases in strain until the sample eventually failed. The displacement vs time curve and resulting force vs displacement curve are shown in Figure S9a-b. This measurement shows that the loading and unloading curve are nearly identical and overlap well. A plot of the resilience and max applied strain against cycle number is shown in Figure S9c. The resilience is calculated as the percent of energy recovered during one cycle normalized by the energy input during that cycle. For this material, all strains showed a resilience of greater than 94% indicating that there is not significant energy loss during deformation.

2.2.2 Uniaxial Compression

Uniaxial compression was performed on a TA.XTPlus Connect Texture Analyzer with a 50 N load cell and monitored with a Dino-Lite Edge Plus AM4117 series 1.3 MP camera. Measurements were performed on circular disks with a diameter of approximately 11.3 mm and heights of approximately 2.6 mm. Samples were compressed between platens lubricated with 100 cSt trimethylsiloxy terminated polydimethylsiloxane at a velocity of 0.1 mm/s (approximate strain rate of 0.038 s^{-1}). Two samples

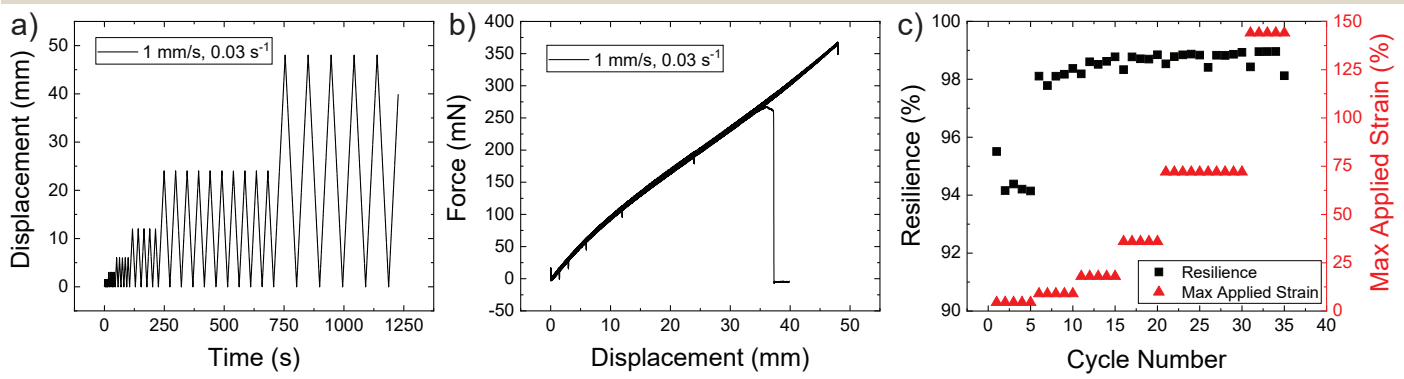

Fig. S9 Plots of a) displacement vs time and b) force vs displacement for cyclic extension measurements. A plot c) of resilience and max applied strain vs cycle number shows that there is not significant energy loss during deformation.

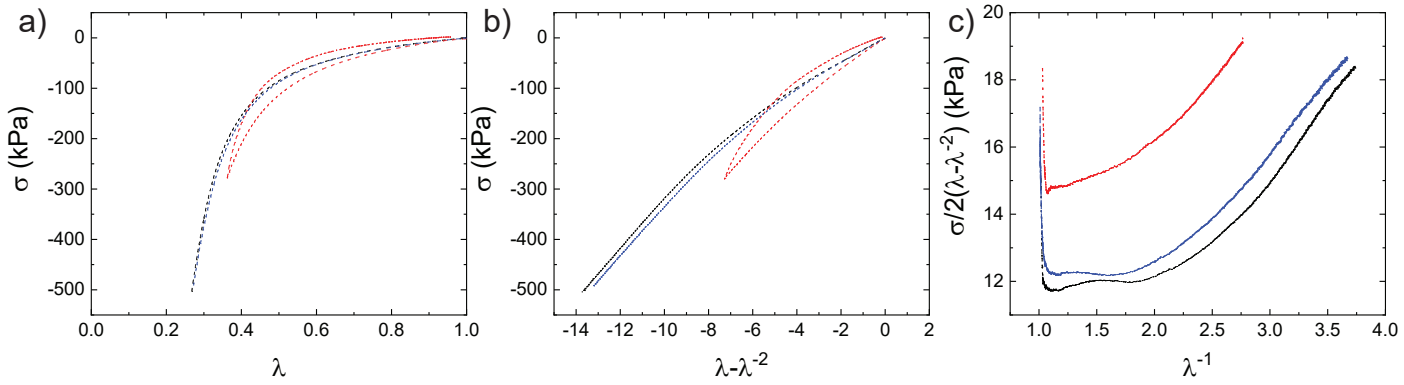

Fig. S10 Plots of the engineering stress σ against a) λ and b) $\lambda - \lambda^{-2}$ for uniaxial compression. Additionally a Mooney plot is contained in c). These tests suggest that this material displays some strain stiffening and little to no dependence on the $\frac{dW}{dI_2}$ term at small strains.

were stopped once the force hit 50 N (the capacity of the load cell employed) while a third sample was stopped at a turnaround displacement of 3.5 mm ($\lambda \approx 0.38$).

Different representations of these measurements in the form of plots of a) the engineering stress σ vs stretch ratio λ, b) σ vs $\lambda - \lambda^{-2}$, and c) $\frac{\sigma}{2(\lambda - \lambda^{-2})}$ vs λ^{-1} are shown in Figure S10. The σ vs λ curve shows similar moduli before increasing in stress. The σ vs $\lambda - \lambda^{-2}$ curve shows that some strain stiffening occurs beyond that predicted by a simple neo-Hookean model. Finally, the Mooney plot shows that the constitutive response has little to no dependence on $\frac{dW}{dI_2}$ at small strains before stiffening.

2.2.3 Fitting a Strain Energy Density Function

Due to the higher-order nonlinearities and the stress stiffening effects, Ogden's hyperelastic strain energy potential has been adopted for characterizing the elastic behavior of the gel. Furthermore, the incompressibility condition was also applied based on the results of the radially confined compression tests. Therefore, the applied strain energy density potential can be expressed using the notation in Abaqus[5,6] as

$$W = \sum_{i=1}^{N} \frac{2\mu_i}{\alpha_i^2} \left(\lambda_1^{\alpha_i} + \lambda_2^{\alpha_i} + \lambda_3^{\alpha_i} - 3\right), \tag{S3}$$

where N denotes the order of the hyperelastic potential, λ_1, λ_2 and λ_3 are the principal stretches, μ_i and α_i are material parameters. The initial shear modulus for Ogden's hyperelastic model becomes

$$\mu_0 = \sum_{i=1}^{N} \mu_i, \tag{S4}$$

which leads for the incompressible case that the Young's modulus is given as

$$E = \sum_{i=1}^{N} 3\mu_i. \tag{S5}$$

For uniaxial (UA) deformations the deformation gradient can be written as

$$\mathbf{F} = \begin{bmatrix} \lambda & 0 & 0 \\ 0 & \lambda_T & 0 \\ 0 & 0 & \lambda_T \end{bmatrix}, \tag{S6}$$

where λ and λ_T are the stretch in the longitudinal and transverse directions, respectively. The right Cauchy–Green deformation tensor can be expressed as

$$\mathbf{C} = \mathbf{F}^T\mathbf{F} = \begin{bmatrix} \lambda^2 & 0 & 0 \\ 0 & \lambda_T^2 & 0 \\ 0 & 0 & \lambda_T^2 \end{bmatrix}. \tag{S7}$$

Due to incompressibility

$$J = \det \mathbf{F} = \lambda\lambda_T^2 \equiv 1 \tag{S8}$$

holds, and thus

$$\lambda_T = 1/\sqrt{\lambda}. \tag{S9}$$

The principal stretches can be obtained as the eigenvalues and eigenvectors of $\mathbf{U} = \sqrt{\mathbf{C}}$, which gives

$$\lambda_1 = \lambda; \qquad \lambda_2 = \lambda_T = \lambda^{-1/2}; \qquad \lambda_3 = \lambda_T = \lambda^{-1/2}. \tag{S10}$$

Based on the strain energy density function the principal Cauchy stresses can be obtained as

$$\sigma_i = \lambda_i \frac{\partial W}{\partial \lambda_i} + p \qquad \text{for} \qquad N = 1,2,3 \tag{S11}$$

where p is the unknown hydrostatic stress that can be determined using the stress-free condition in the transverse directions, namely $\sigma_2 = \sigma_3 \equiv 0$. After substituting Equation (S3) into Equation (S11), the principal Cauchy stress solutions for uniaxial loading can be expressed as

$$\sigma_1 = \sum_{i=1}^{N} \lambda_1 \frac{2\mu_i}{\alpha_i} \left(\lambda_1^{\alpha_i - 1}\right) + p, \tag{S12}$$

$$\sigma_2 = \sigma_3 = \sum_{i=1}^{N} \lambda_T \frac{2\mu_i}{\alpha_i} \left(\lambda_T^{\alpha_i - 1}\right) + p. \tag{S13}$$

Using the condition that $\sigma_2 = \sigma_3 \equiv 0$ and substituting into Equation (S10) the unknown hydrostatic pressure can be obtained as

$$p = -\sum_{i=1}^{N} \lambda_T \frac{2\mu_i}{\alpha_i} \left(\lambda_T^{\alpha_i - 1}\right) = -\sum_{i=1}^{N} \lambda^{-1/2} \frac{2\mu_i}{\alpha_i} \left(\lambda^{1/2 - \alpha_i/2}\right). \tag{S14}$$

Substituting back into Equation (S12) gives the incompressible

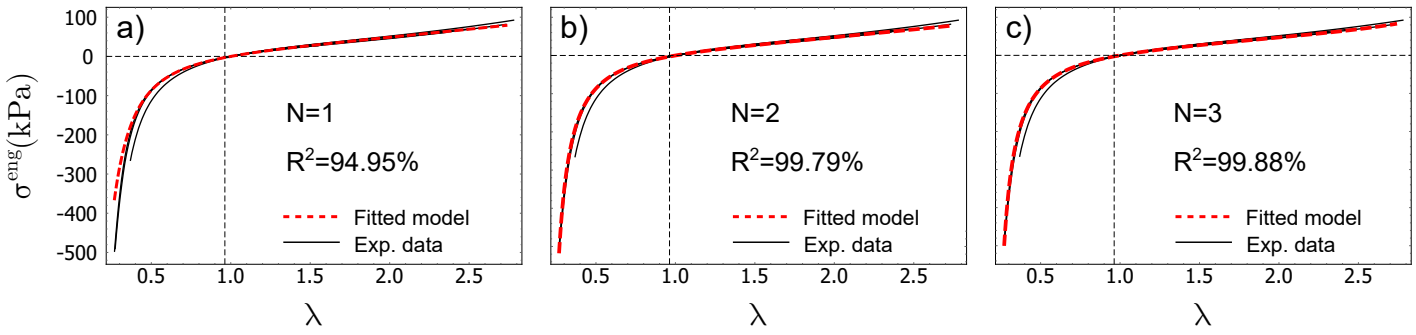

Fig. S11 The accuracy of the hyperelastic model fitting (total number of measurement points: 354; including 3 compression and 5 tensile test curves)

Cauchy stress solution for uniaxial loading, namely

$$\sigma_1 = \sum_{i=1}^{N} \frac{2\mu_i}{\alpha_i} \left(\lambda^{\alpha_i} - \lambda^{-\alpha_i/2} \right). \tag{S15}$$

Using the relation between the first Piola–Kirchhoff (engineering) stress ($\mathbf{P}$) and the Cauchy stress (σ), namely $\mathbf{P} = J\sigma\mathbf{F}^T$ gives that the incompressible first Piola–Kirchhoff stress solution for uniaxial loading can be written as

$$P_1 = \sigma_1/\lambda, \tag{S16}$$

from which the engineering stress solution becomes

$$\sigma^{\text{eng}} = P_1 = \sum_{i=1}^{N} \frac{2\mu_i}{\alpha_i} \left(\lambda^{\alpha_i - 1} - \lambda^{-\alpha_i/2 - 1} \right). \tag{S17}$$

Hereafter, the material parameters of Ogden's hyperelastic potential were fitted to the uniaxial engineering stress curves for both tension and compression (see Figure S11). The quality function was defined as the Mean Squared Difference (MSD), namely

$$Q = \frac{1}{K} \sum_{k=1}^{K} \left(\sigma_k^{\text{eng,exp}} - \sigma^{\text{eng}}(\lambda_k^{\text{exp}}) \right)^2, \tag{S18}$$

where k stands for the number of captured data points in uniaxial tests. The global minimization of the quality function using the Nelder-Mead optimization algorithm.[7] The accuracy of the models could be quantified by the coefficient of determination R^2, which is defined as

$$R^2 = 1 - \frac{\sum_{i=1}^{M} \left(f_i^{\text{meas}} - f_i^{\text{fit}} \right)^2}{\sum_{i=1}^{M} \left(f_i^{\text{meas}} - \bar{f} \right)^2} \tag{S19}$$

where f stands for the quantity to be compared, while $\bar{f}$ is its average value. The value of R^2 should satisfy $0 < R^2 \leq 1$, where $R^2 = 1$ represents the perfect fit.[8]

The results of the parameter fitting to 3 compression and 5 tensile test curves (with $K = 354$ data point) clearly show that the Ogden's hyperelastic model is capable of characterizing the uniaxial elastic behavior of the gel. The accuracy of the first-order ($N = 1$) model is acceptable, however at elevated compressive strains the deviation from the measurement curve increases. However, the second and third-order model shows excellent fitting only with minor adjustment in the parameters. The fitted material parameters and the corresponding statistics for the fitting procedures are listed in Table S3. The quality function also indicates shows that the mean squared difference is 0.02501 kPa for the first-order fitting and 0.02255 and 0.02235 for the second- and third-order fits, respectively.

Table S3 Summary of the fitted material parameters using Ogden's hyperelastic potential and the fitting statistics

Model order N	μ_1 (kPa)	α_1 (-)	μ_2 (kPa)	α_2 (-)	μ_3 (kPa)	α_3 (-)	Q (kPa)	R^2 (-)	Fitting time (s)
1	24.828	2.3712	-	-	-	-	0.02501	94.95%	2.09
2	24.364	2.3873	0.0764	-5.5977	-	-	0.02255	99.79%	25.65
3	24.558	2.3033	0.0601	-5.8438	0.001353	11.6049	0.02235	99.88%	197.508

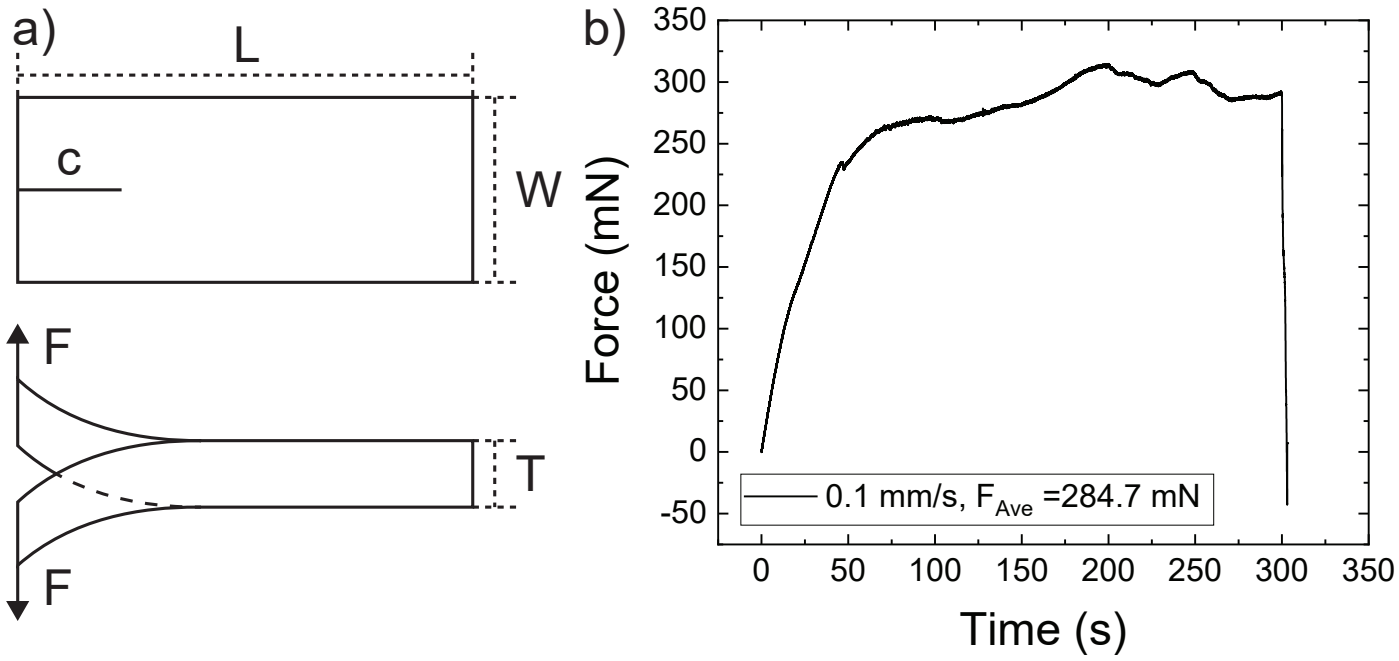

Fig. S12 Schematic of the sample geometry and an example force vs time curve for the tear test performed at 0.1 mm/s.

2.3 Tear Tests

Tear tests were performed on a TA.XTPlus Connect Texture Analyzer with a 50 N load cell. Trouser samples where the legs are pulled in opposite directions out-of-plane where used, as shown in Figure S12A. In this geometry, the average propagation force F_{Ave} can be related to the fracture energy G_c through the sample thickness T.[9]

$$G_c = \frac{2F_{Ave}}{T} \tag{S20}$$

This relation assumes that deformation in the legs is negligible. A schematic and plot of example data fort this test is contained in Figure S12. F_{Ave} is calculated by averaging the force values only during the crack propagation stage. Summary of the data gathered is contained in Table S6.

Table S4 Summary of the tear tests that were performed on trouser samples.

Sample	Displacement Rate (mm/s)	c (mm)	L (mm)	W (mm)	T (mm)	F_{Ave} (mN)	G_c (N/m)
0.1-1	0.1	27.1	89.2	49.4	2.85	272.6	191.3
0.1-2	0.1	27.9	88.5	46.6	3.2	284.7	177.9
0.1-3	0.1	29.4	89.3	48.4	2.77	262.2	189.3
1-1	1	25.1	88.3	50.3	2.83	435.2	307.6
1-2	1	25.9	87.8	48.9	2.1	360.2	343.0
1-3	1	23.5	88.3	50.6	2.8	341.7	244.1
1-4	1	28.7	87.5	50.3	3.2	365.5	228.4
10-1	10	23.9	86.9	47.6	2.9	505.8	348.8
10-2	10	–	87.8	52.2	2.6	515.1	396.2
10-3	10	24.4	87.6	49.5	3.1	574.9	370.9

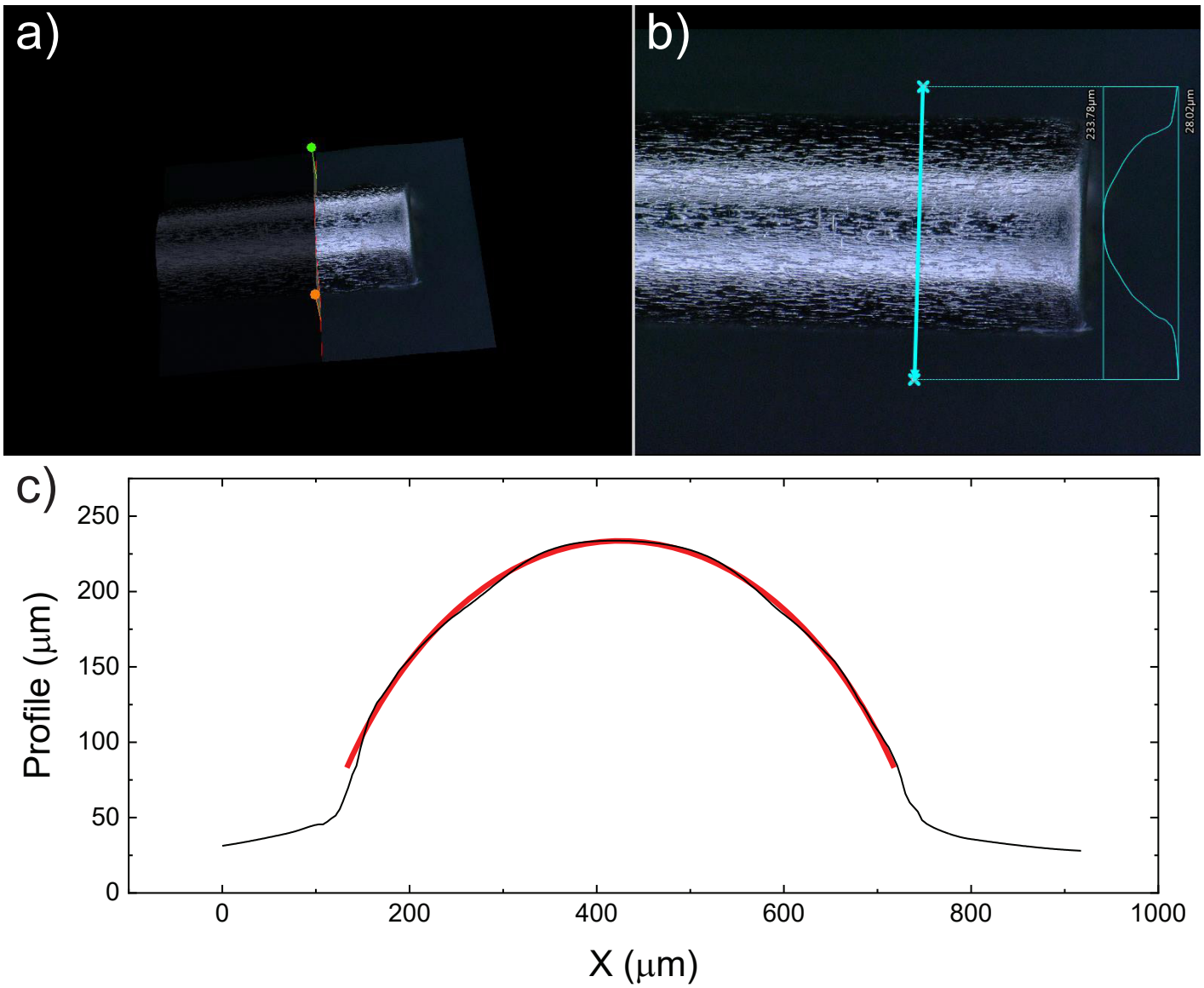

Fig. S13 Surface scan and line profile of the walls of the needle used in this study. Fitting this curvature shows that the needle radius is $a = 359.3 \pm 0.7$ μm (red fit).

2.4 Needle Tip Profile

Profiles of the needle walls and corner at the needle tip were gathered on a Keyence VHS-5000 Microscope. A profile of the needle wall is contained in Figure S13. The surface images in Figure S13a-b show that the needle walls have a particular texture. The needle was used as received and so this texture must develop during the manufacturing process. A circular fit to the profile in Figure S13c estimated the outer needle radius as $a = 359.3 \pm 0.7$ μm which is rounded to 0.359 mm in the main text. A profile of the corner at the needle tip is shown in Figure S14. Fits to this profile suggest that the outside corner of the needle has a radius of 80.5 ± 1.1 μm and the inside corner has a radius of 55.7 ± 0.4 μm.

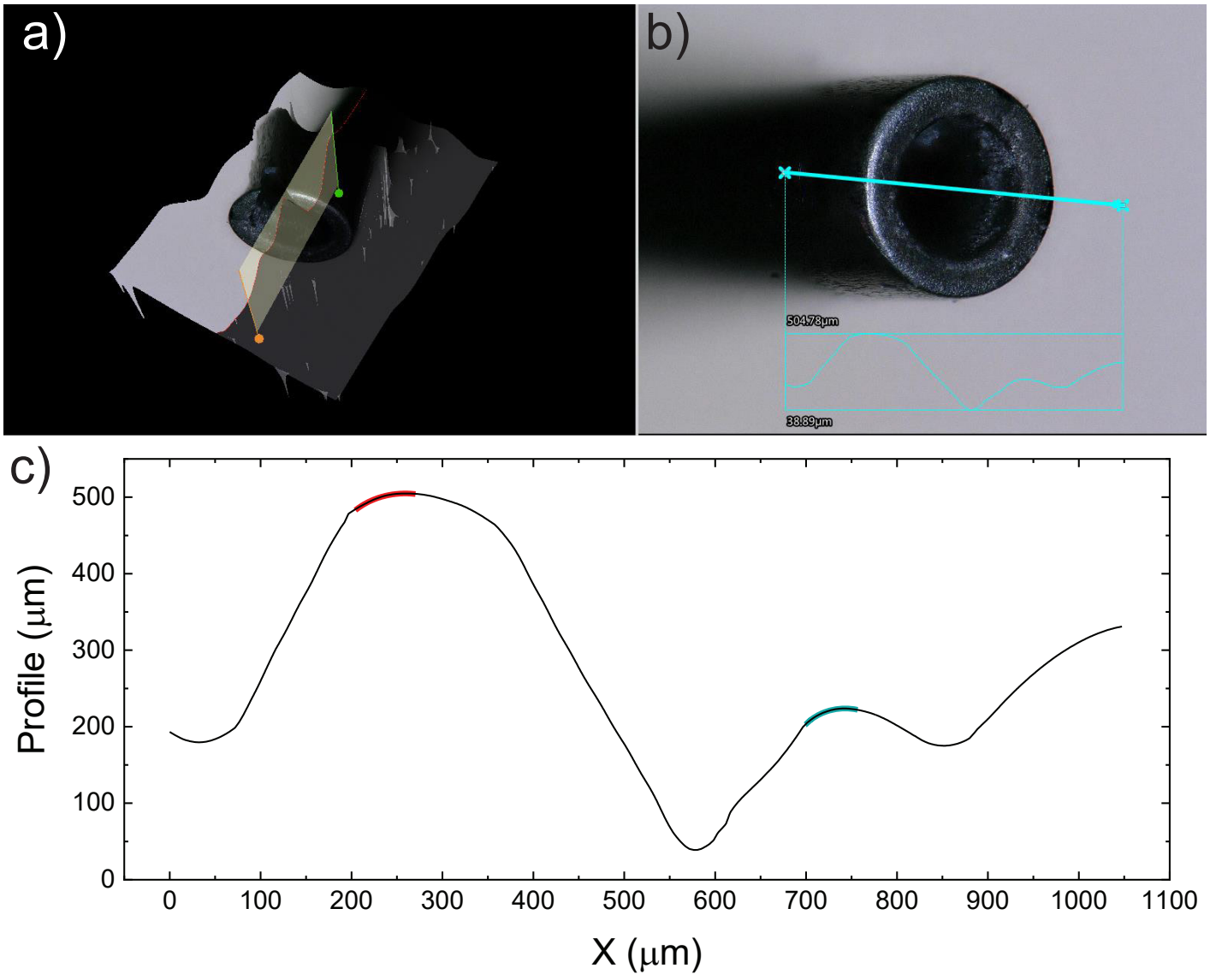

Fig. S14 Surface scan and line profile of the corner at the needle tip. Fits to the profile assuming a circular geometry suggest that the outer corner profile has a radius of 80.5 ± 1.1 μm (red fit) while the inner corner profile has a radius of 55.7 ± 0.4 μm (blue green fit).

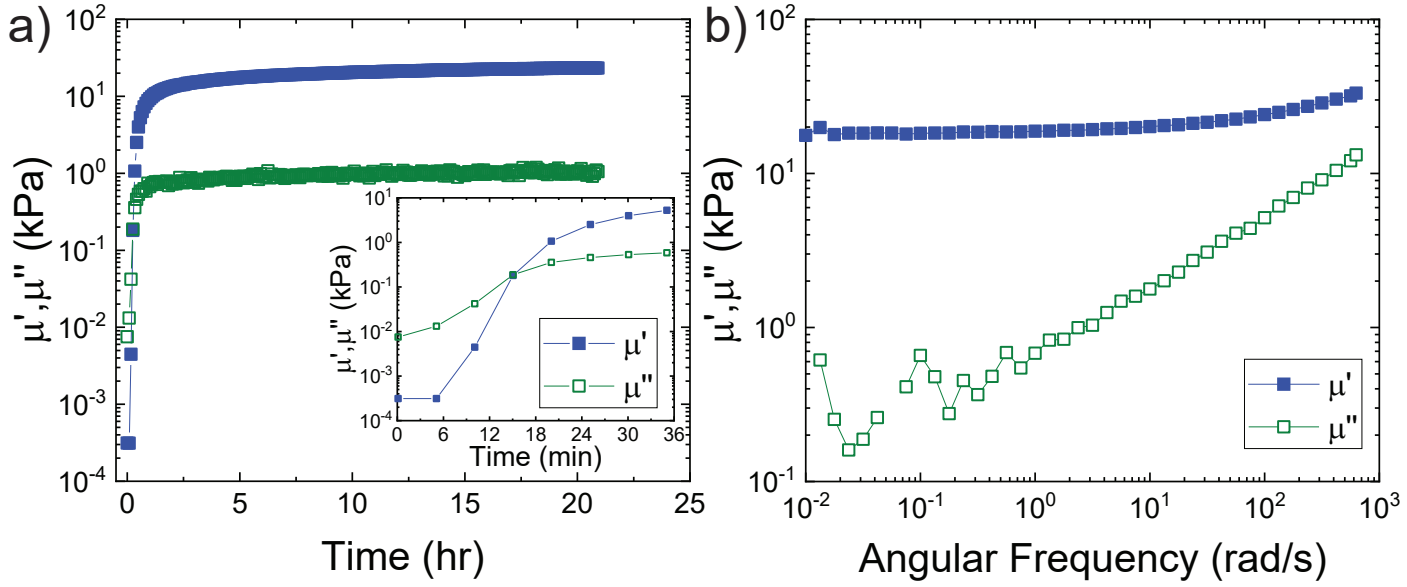

Fig. S15 a) Plot of the storage and loss moduli vs time spent at 70°C during curing of the material. b) Frequency sweep of the same sample after equilibrating at 25°C for 2 hours.

2.5 Rheometry

Oscillatory measurements to monitor curing and quantify the rheological response of the blend used in this study was performed on a TA Instruments AR-G2 stress-controlled rheometer with a 40 mm steel parallel plate geometry with a gap of 400 μm. Uncured material was loaded into the rheometer at room temperature. The temperature was then increased to 70°C and held at this temperature while the curing was monitored by measuring the moduli at a frequency of 10 rad/s and strain amplitude of 0.1% every 5 minutes for 21 hours. After 21 hours, the sample was equilibrated to 25°C for 2 hours. Finally, a frequency sweep was performed from 0.01 rad/s to 628.319 rad/s with an amplitude of 0.1% strain.

A plot of the shear storage μ' and loss μ'' moduli during the curing process is shown in Figure S15a. The gel point, defined as the point at which $\mu' = \mu''$, occurs at approximately 15 minutes as seen in the inset. The material continues to cure before the μ' and μ'' appear to level off at long cure times as the catalyst diffuses about the system and crosslinks the reactants together to form network junctions. This suggests that the 21 hours that the material cures at high temperature gives sufficient time for the curing reaction to proceed to the point that, even though the catalyst remains active at room temperature, we would not expect to observe a significant increase in the stiffness of the material due to the formation of further network junctions at room temperature. A plot of μ' and μ'' against frequency is contained in Figure S15b. This plot shows that the μ' that develops is fairly independent of frequency and slightly increases at frequencies above 10 rad/s. E is estimated from the average of $3\mu'$ up to 10 rad/s as 58.1 ± 4.3 kPa. In this frequency range $\mu' >> \mu''$.

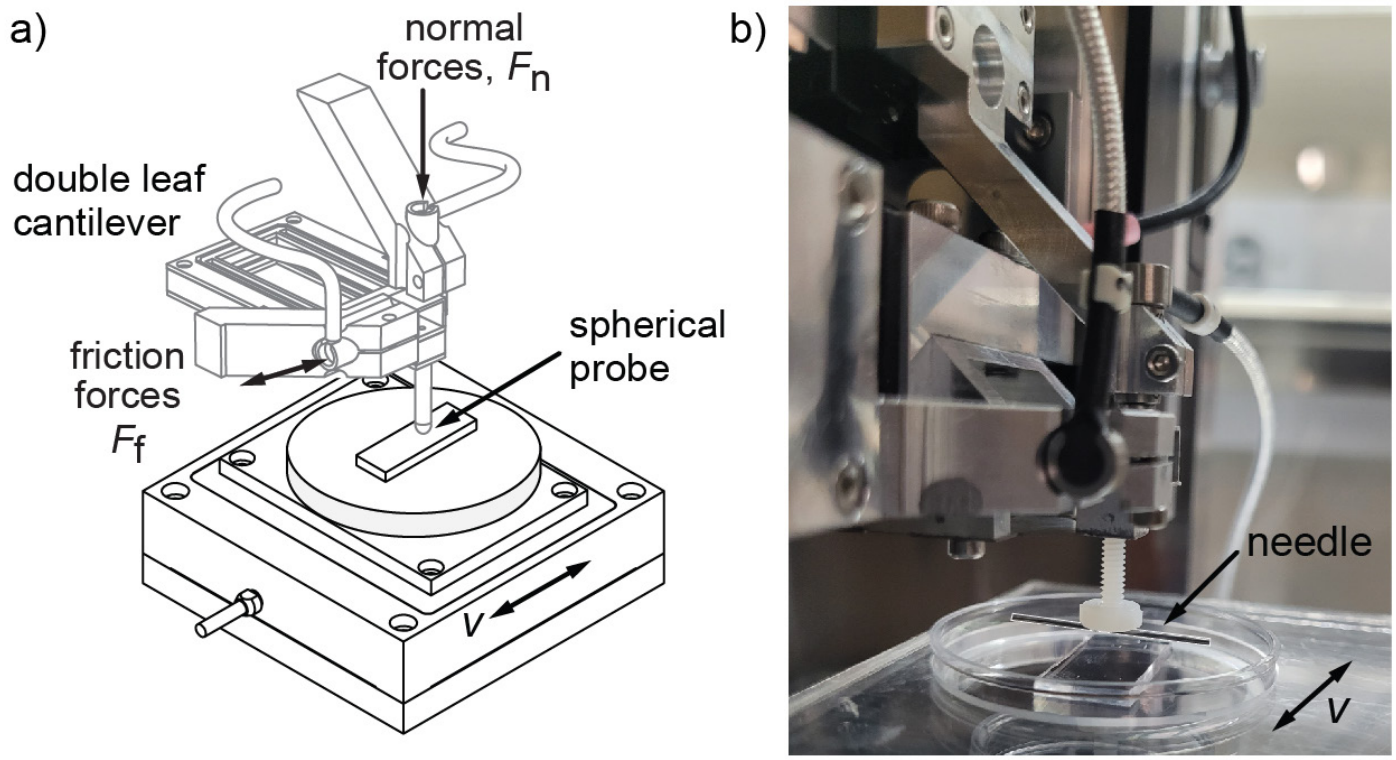

Fig. S16 a) Schematic and b) image of the linear reciprocating tribometer[10] employed in this work to measure sliding friction. The needle is perpendicular to the direction of reciprocation.

2.6 Sliding Friction Measurements

Sliding experiments were conducted with a custom-built linear reciprocating tribometer, as shown in Figure S16. A chrome steel spherical probe (radius of curvature, a = 2.38 mm) and a 22 gauge blunt-tipped steel needle (outer radius, a = 0.355 mm measured via calipers) were mounted to a double-leaf cantilever with normal and tangential spring constants of 180 μN/μm and 525 μN/μm, respectively. The needle was attached horizontally to the cantilever such that the long axis was perpendicular to the sliding direction (Figure S16b). Silicone samples (10 mm wide) were placed on a motorized stage (Physik Instrumente, L-509.20DG10, 52 mm travel range), and the friction coefficient was measured at four different sliding speeds (v = 0.1, 0.5, 1, 2 mm/s). With the spherical probe, three normal forces (F_n = 0.5, 1, 2.5 mN) were applied for a sliding path, l, (1/2 cycle) of 3 or 4 mm, depending on the normal force. The sliding paths were chosen to ensure that the sliding distance in one direction was at least eight times the estimated Hertzian contact area radius at maximum normal load. For the steel needle, a cylinder-on-flat geometry was used to estimate the rectangular contact area and applied pressure across five normal forces (F_n = 0.5, 1, 2.5, 3.1, and 5 mN) along l = 3 mm. The estimated maximum contact pressures at the center of contact for both probe geometries can be found in Table S5 and were calculated using Equation (S21) and Equation (S22).[11]

Table S5 Summary of the estimated maximum contact pressures at the center of contact for the two different probe geometries.

Probe geometry	a (mm)	Force (mN)	Estimated contact pressure (kPa)
Spherical probe	2.38	0.5	4.58
		1	5.77
		2.5	7.83
Needle	0.355	0.5	1.83
		1	2.59
		2.5	4.10
		3.1	4.57
		5	5.80

$$P_{sphere} = \frac{1}{\pi}\left(\frac{6FE^{*2}}{a^2}\right)^{\frac{1}{3}} \quad \text{(S21)}$$

$$P_{cylinder} = \left(\frac{FE^*}{\pi La}\right)^{\frac{1}{2}} \quad \text{(S22)}$$

Friction coefficients were calculated by averaging the normal and friction forces within the middle 25% of the sliding path, as depicted in Figure S17 with a representative friction force loop. The following equation (Equation (S23)) was used to calculate the average friction coefficient for each cycle, f_{cycle}, where $F_{f,forward}$ is the average friction force in the forward direction and $F_{f,reverse}$ is the average friction force in the reverse direction. The reported friction coefficients and standard deviations for each normal load were determined by averaging f_{cycle} over 100 cycles to obtain f.

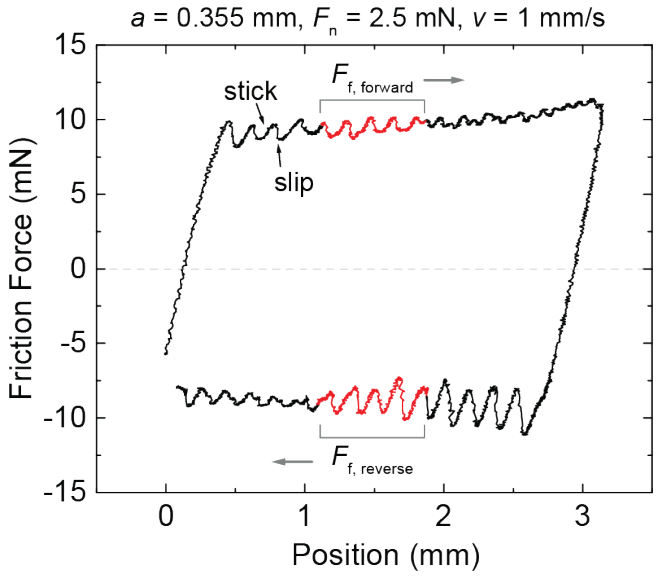

Fig. S17 Representative friction force loop for the needle at an applied normal force of 2.5 mN and a velocity of 1 mm/s. The middle 25% of the friction force in both the forward and reverse direction (denoted by brackets and highlighted in red) is used to calculate the friction coefficient. Note that the peaks and valleys that are present in the free-sliding region indicate that stick-slip is occurring during sliding.

$$f_{cycle} = \frac{< F_{f,forward} > - < F_{f,reverse} >}{2 < F_n >} \tag{S23}$$

Friction coefficients as a function of applied normal force and maximum contact pressure for the spherical probe and needle are displayed in Figure S18. The friction coefficient, f, decreases with increasing normal load and pressure and generally increases with increasing sliding velocity. Stick-slip also increases with increasing velocity (Figure S19).

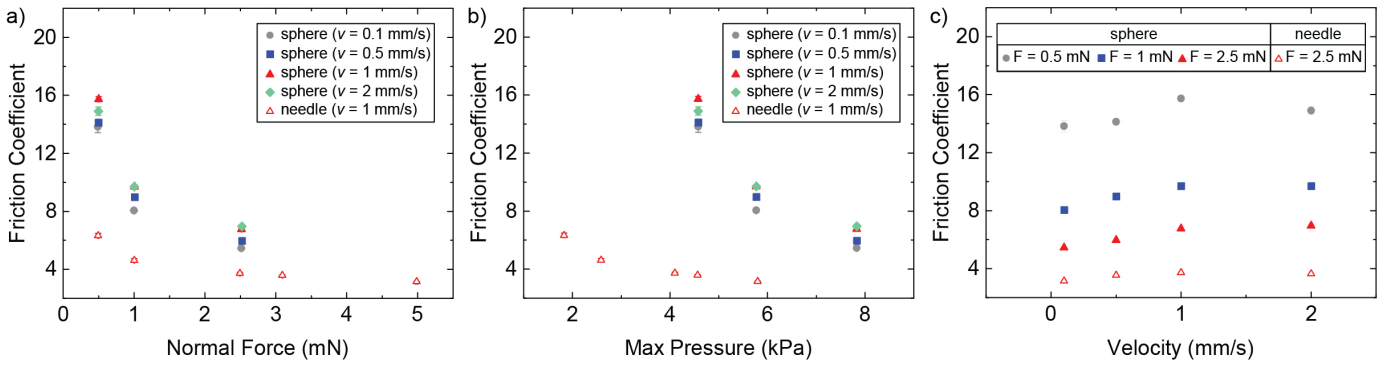

Fig. S18 Plots of the friction coefficient against a) normal force, b) max contact pressure at the center of contact, and c) sliding velocity. These measurements show that the friction coefficient decreases with increasing normal force and max pressure. The friction coefficient appears to increase slightly with sliding velocity, but more rigorous studies need to be conducted to make any conclusions.

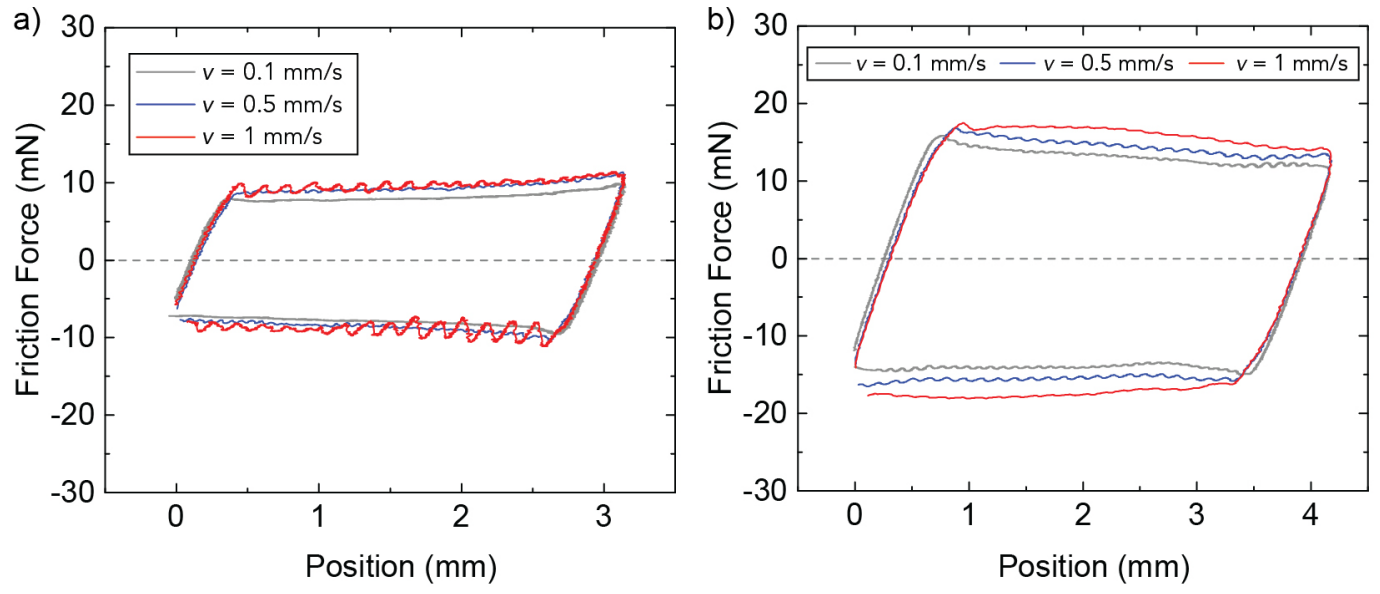

Fig. S19 Friction force loops for the a) needle and b) sphere probe geometries at various sliding velocities at an applied normal force of 2.5 mN. For the needle probe, as the sliding speed increased, the stick-slip behavior increased.

Table S6 Summary of the friction coefficient measurements performed in this work.

Probe	a (mm)	Velocity (mm/s)	F_n (mN)	f
Chrome Steel Sphere	2.38	0.1	0.5	13.8 ± 0.4
Chrome Steel Sphere	2.38	0.5	0.5	14.1 ± 0.2
Chrome Steel Sphere	2.38	1	0.5	15.7 ± 0.2
Chrome Steel Sphere	2.38	2	0.5	14.9 ± 0.3
Chrome Steel Sphere	2.38	0.1	1	8.05 ± 0.07
Chrome Steel Sphere	2.38	0.5	1	8.99 ± 0.06
Chrome Steel Sphere	2.38	1	1	9.70 ± 0.09
Chrome Steel Sphere	2.38	2	1	9.71 ± 0.11
Chrome Steel Sphere	2.38	0.1	2.5	5.44 ± 0.06
Chrome Steel Sphere	2.38	0.5	2.5	5.98 ± 0.03
Chrome Steel Sphere	2.38	1	2.5	6.77 ± 0.05
Chrome Steel Sphere	2.38	2	2.5	6.97 ± 0.10
Steel Needle	0.359	1	0.5	6.33 ± 0.15
Steel Needle	0.359	1	1	4.62 ± 0.12
Steel Needle	0.359	0.1	2.5	3.16 ± 0.02
Steel Needle	0.359	0.5	2.5	3.54 ± 0.02
Steel Needle	0.359	1	2.5	3.73 ± 0.06
Steel Needle	0.359	2	2.5	3.65 ± 0.05
Steel Needle	0.359	1	3.1	3.58 ± 0.03
Steel Needle	0.359	1	5	3.15 ± 0.02

References

1 K. R. Shull, D. Ahn, W.-L. Chen, C. M. Flanigan and A. J. Crosby, *Macromolecular Chemistry and Physics*, 1998, **199**, 489–511.

2 C. W. Barney, M. E. Helgeson and M. T. Valentine, *Extreme Mechanics Letters*, 2022, **52**, 101616.

3 R. S. Rivlin and D. W. Saunders, *Philosophical Transactions of the Royal Society A: Mathematical, Physical and Engineering Sciences*, 1951, **243**, 251–288.

4 M. Destrade, G. Saccomandi and I. Sgura, *Proceedings of the Royal Society A*, 2017, **473**, 20160811.

5 *Abaqus*.

6 G. A. Holzapfel, *Nonlinear Solid Mechanics: A Continuum Approach for Engineering*, 2000.

7 A. Kossa and S. Berezvai, *Polymer Testing*, 2016, **53**, 149–155.

8 S. Berezvai, *Constitutive modelling of compressible solids including viscoelastic/viscoplastic effects*, 2020.

9 G. J. Lake, *Rubber Chemistry and Technology*, 1995, **68**, 435–460.

10 J. M. Urueña, S. M. Hart, D. L. Hood, E. O. McGhee, S. R. Niemi, K. D. Schulze, P. P. Levings, W. G. Sawyer and A. A. Pitenis, *Tribology Letters*, 2018, **66**, 1–7.

11 K. L. Johnson, *Contact Mechanics*, Cambridge University Press, 1985.